European Conference on Computational Fluid Dynamics
ECCOMAS CFD 2006
P. Wesseling, E. Oñate and J. Périaux (Eds)

COMPUTATION OF AERODYNAMIC NOISE FROM ROD WAKE-AIRFOIL INTERACTIONS

Sven Peth*, Jung H. Seo†, Young J. Moon†, Marc C. Jacob‡, and Frank Thiele*

*Technische Universität Berlin
Institut für Strömungsmechanik und Technische Akustik
Müller-Breslau-Straße 8, 10623 Berlin, Germany
e-mail: sven.peth@cfd.tu-berlin.de, frank.thiele@cfd.tu-berlin.de,
web page: http://www.cfd.tu-berlin.de

†Korea University
Department of Mechanical Engineering
1 Anam-dong, Sungbuk-ku, Seoul, 136-701, Korea
e-mail: jhseo@korea.ac.kr, yjmoon@korea.ac.kr
web page: http://cfd.korea.ac.kr

‡Ecole Centrale de Lyon
Centre Acoustique du LMFA, UMR CNRS 5509
69134 Ecully Cedex, France
e-mail: marc.jacob@ec-lyon.fr
web page: http://acoustique.ec-lyon.fr

Key words: rod-airfoil, large eddy simulation, CAA, LPCE, far-field acoustics

Abstract. *Aerodynamic noise from the rod wake-airfoil interactions at M=0.2 and Re_D=46,000 is computed by solving the linearized perturbed compressible equations (LPCE)[1], with the acoustic source and hydrodynamic flow variables computed from the incompressible LES. A 2D LPCE calculation is conducted at zero spanwise wave-number (k_z=0) with an assumption of statistical homogeneity in the spanwise direction. Then, a 2D Kirchhoff method is used to extrapolate the sound field at the acoustic far-field boundary (40D) up to the microphone location (185D away from the airfoil chord center). Finally, a power spectrum density (PSD) for actual span (30D) is predicted by Oberai's correction method for 3D spectral acoustic pressure and spanwise coherence function for the wall pressure. The computational results for flow and acoustics are critically validated with the experimental data[2] measured at the Ecole Centrale de Lyon.*

1 INTRODUCTION

The interaction of vortices with structures is one important factor in industrial design, because it creates noise. And reduction of noise is a sales argument for many products,

e.g. a notebook fan, automobiles, airplanes, and etc. The way of reducing it is strongly connected with understanding its sources. There are two types of noise components. The tonal part that is connected to periodical processes. And the broadband noise that is very often an interaction of many components cannot be deterministically analyzed. The rod-airfoil configuration is a simple benchmark setup for the study of vortex interaction noise. The experimental setup for turbo-engines or helicopter rotors is too complex for finding basic mechanisms. The rod acts as vortex generator and creates a Karman vortex street which hits the airfoil. And the properties of the flow past the rod were investigated.

In the present study, a hydrodynamic acoustic splitting method is applied to a rod-airfoil configuration at M=0.2. First, a three-dimensional large eddy simulation (LES) computes the hydrodynamic properties. It might seem odd that an incompressible solver is used for noise prediction, but the only source for the acoustics are the total pressure changes in the flow which can be obtained by an incompressible LES. Second, the two-dimensional acoustic field is calculated by the linearized perturbed compressible equations (LPCE)[1]. Subsequently, there is a 2D Kirchhoff extrapolation to the far-field and a 3D correction after Oberai[5]. An important advantage in the splitting is the computational efficiency. The LES is in 3D, but the LPCE is performed as 2D. Both solvers are independent from each other, they even use different grids which are optimized for their particular needs.

The investigation of rod-airfoil configurations has a short history which means there is only little literature, yet, for example by Sorgüven et al.[9] and Magagnato et al.[10] or Boudet[12]. This work uses experimental results by Jacob[2] as reference in a similar configuration. On the other hand the flow past cylinders has been studied since Strouhal[11] in 1878. And also the unsteady behaviour of airfoils is examined since Glauert[13] in 1929, or more recent by Goldstein[14]. The objectives of this study are not only to evaluate critically the computational methodology proposed by Seo and Moon[1] by comparing the hydrodynamic and aeroacoustic results with the experiment[2] measured at Ecole Centrale de Lyon but also to understand the governing physics to identify the noise sources.

2 COMPUTATIONAL GRID

The dimensions of the computational domain aligns to the experimental setup by Jacob[2]. It includes a rod and a NACA0012 airfoil in tandem configuration. The governing flow parameters are Re_D=46,000 and M=0.2. All computations use nondimensional values, but for experimental comparison it is necessary to provide them with units. The rod diameter D is equal to 10 mm, the inflow velocity $u_\infty = 72\,\mathrm{m/s}$, the ambient temperature $T_0 = 293\,\mathrm{K}$ and the ambient pressure $p_0 = 98.9\,\mathrm{kPa}$. There is a small offset between the centers of the rod and airfoil, because in technical applications it is more likely that vortices are not symmetric to the airfoil chord. The trailing edge of the airfoil is rounded with a radius, thus the chord length is 99 mm instead of 100 mm.

Different grids were used for hydrodynamic and acoustic calculations. The hydrodynamic computation is performed by an incompressible LES in 3D and employs 3.14

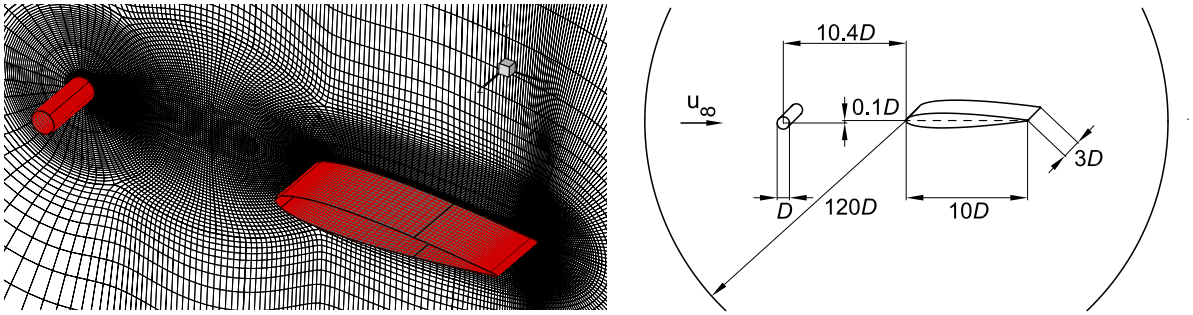

Figure 1: Computational domain, left: 3D mesh of LES with every other grid point plotted; right: sketch of relative dimension.

million grid cells with 32 blocks (30 cells used in the spanwise direction). The grid in the wake region is designed to be homogeneous to avoid quick diffusion of the vortices. The grid size is chosen that a vortex is resolved by 20 cells. The nondimensional wall distance y^+ of the airfoil is rather large with a value of 12.5 and some near-wall turbulence physics are not resolved with the present grid. As far as noise prediction is concerned, the present grid resolution may be not too off because main noise comes from the large scale motions of the eddies. Due to the large y^+ the largest ratio of wall cell length to thickness is 47. The hydrodynamic domain has the shape of a cylinder with a diameter of $240D$. All outer boundaries are defined as inflow, the body boundaries are set to no slip, and periodic boundaries are used in spanwise direction.

The acoustic grid consists of 0.16 million cells in 6 blocks. It is an overlaid grid which makes it very easy to fit perfectly to the body contour. The grid in the wake region and around the bodies is coarser than the hydrodynamic grid, because the aeroacoustic and hydrodynamic calculation use the same time step, but the acoustic information propagates with the speed of sound while the flow propagates roughly with u_∞. The domain of the acoustic calculation is a circle of $120D$, and it is relatively fine at the outer boundary compared to the hydrodynamic grid. The outer grid size has been chosen in order to resolve the wavelength of an acoustic wave with 10 kHz with 7 cells.

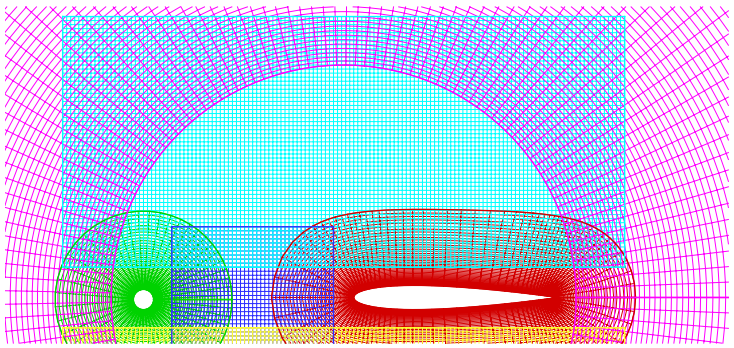

Figure 2: 2D mesh for acoustic calculation, every other grid point depicted.

3 HYDRODYNAMICS

The main idea is to split the whole computation into a hydrodynamic and an acoustic part. The hydrodynamic computation is performed by an incompressible large eddy simulation (iLES) while the acoustic computation uses the linearized perturbed compressible equations[1] (LPCE). Therefore the instantaneous total flow variables are decomposed into the incompressible and perturbed compressible variables.

$$\begin{aligned} \rho(\vec{x},t) &= \rho_0 + \rho'(\vec{x},t) \\ \vec{u}(\vec{x},t) &= \vec{U}(\vec{x},t) + \vec{u}'(\vec{x},t) \\ p(\vec{x},t) &= P(\vec{x},t) + p'(\vec{x},t) \end{aligned} \tag{1}$$

The compressible variables represent the unsteady viscous flow, while the perturbed compressible variables describe the acoustic fluctuations and all other compressible components. The exclusion of compressibility in the Navier-Stokes equations for the iLES leads to the incompressible Navier-Stokes equations. Their filtered form is written as

$$\frac{\partial \tilde{U}_j}{\partial x_j} = 0, \tag{2}$$

$$\rho_0 \frac{\partial \tilde{U}_i}{\partial t} + \rho_0 \frac{\partial}{\partial x_j}\left(\tilde{U}_i \tilde{U}_j\right) = -\frac{\partial \tilde{P}}{\partial x_i} + \mu_0 \frac{\partial}{\partial x_j}\left(\frac{\partial \tilde{U}_i}{\partial x_j} + \frac{\partial \tilde{U}_j}{\partial x_i}\right) - \rho_0 \frac{\partial}{\partial x_j} M_{ij} \tag{3}$$

where the resolved states are marked by ($\tilde{}$). There are many ways to model the sub-grid tensor M_{ij}. One aspect of this work is to reduce the computational effort, consequently the tensor is set to zero, i.e. the sub-scale turbulence is not modeled.

The iLES is solved by an iterative implicit fractional step method (Poisson's equation for pressure). The momentum equations are time-integrated by a four stage Runge-Kutta method and spatially discretized by a sixth-order compact finite difference[3] scheme. Then the pressure field is iteratively solved to satisfy continuity, and the velocity is updated by a correction step. The results of the iLES act as source for the LPCE. Consequently, the spanwise average of the results have to be saved for every time step. The computation covers 50 cycles of Karman vortex shedding of the rod to have reasonable spectral-statistics.

Two isosurfaces of the instantaneous vorticity are plotted in Figure 4. The three-dimensional character of the flow is clearly visible. There are three sources for vorticity, the rod, the leading edge and the trailing edge of the airfoil. The strongest source is the rod which also creates a Karman vortex street that hits the leading edge of the airfoil. The vortex shedding of the cylinder is very unsteady. The intensity of the eddies differs strongly in time which can be seen in Figure 4 left.

The lift and drag of the cylinder oscillates as the eddies emerge. There are phases of weak and strong amplitudes. The same Figure depicts also the coefficients of the airfoil. It is directly observable that the lift of rod and airfoil oscillate with the same frequency.

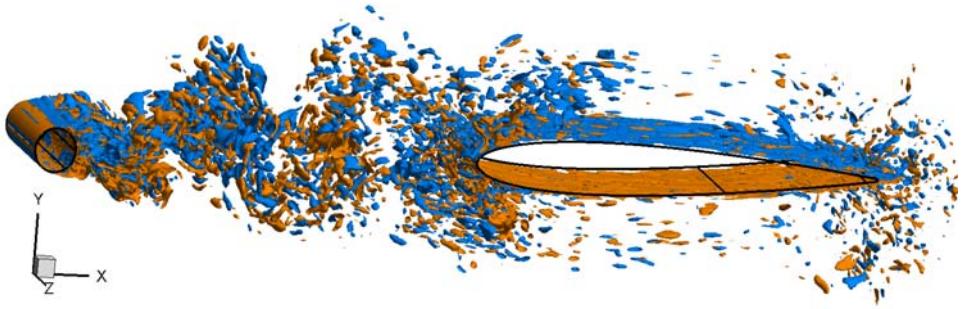

Figure 3: Instantaneous vorticity with isosurfaces at $\omega D/u_\infty = -3$ and $\omega D/u_\infty = 3$.

A spectral analysis of them is plotted in Figure 4 right. The power spectrum densities (PSD) of the lift coefficients are in very good agreement over the whole bandwidth with a peak at a $St \approx 0.185$ which corresponds to the rod shedding frequency and the primary acoustic tone. The vortex shedding induces a periodic marching of the stagnation point at the leading edge. Hence, the stagnation pressure changes periodically form upper side to lower side of the airfoil. This marching affects the forces acting on the airfoil, but more important it creates the primary acoustic tone. The marching has a similar impact as a change in the angle of attack. A big difference between them is that the shedding has less spacial influence, because its mass flow is rather small. This behaviour can be seen when the marching of the stagnation point reaches the turning point on the lower side of the airfoil. An airfoil with an angle of attack of 35° would have its stagnation point on a similar position, but the flow would separate on the upper side. There is no separation area in a rod-airfoil configuration. A low pressure region appears on the upper side, but it is smaller, because the mass flow of the deflected flow is small and the flow outside of the wake helps to relax the pressure. Another reason is that the marching proceeds with a high frequency which causes strong mixing in flow and boundary layer.

Figure 4 depicts the drag of rod and airfoil, too. It appears to be surprising that the

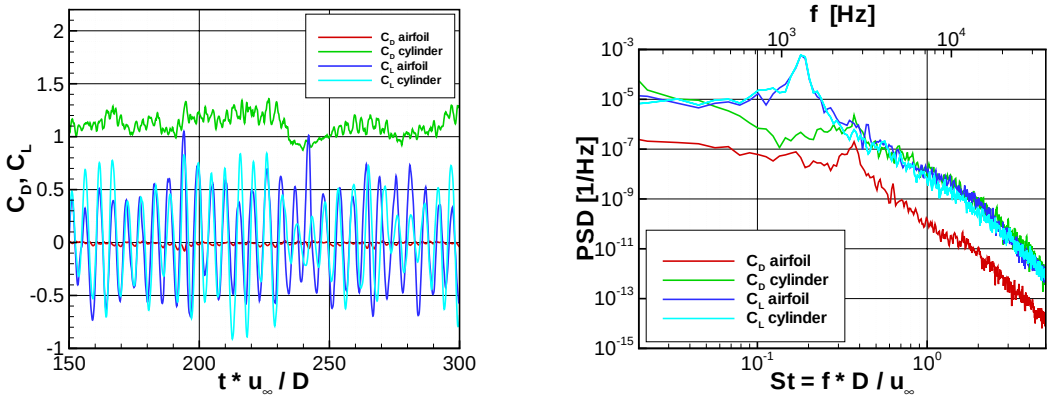

Figure 4: Lift and drag coefficients of cylinder and airfoil, left: variation in time; right: spectral analysis.

drag of the airfoil is zero or even negative. This effect arises, because the leading edge is in the wake region with a low pressure while the trailing edge is dominated by the ambient pressure. The time signals of cylinder and airfoil differ strongly, but the PSD shows that both have a peak at twice the shedding frequency. The PSD of the rod has a higher level, and the airfoil's PSD has a more distinctive peak.

4 ACOUSTICS

The aeroacoustic field at zero spanwise wave number k_z=0 is obtained by solving the linearized perturbed compressible equations (LPCE). The only acoustic source is DP/Dt from the iLES solution. The interpolation from hydrodynamic to acoustic grid is performed by a Lagrangian interpolation method. The far-field sound pressure is extrapolated by a 2D Kirchhoff method in frequency domain. The acoustic pressure in mid-span plane has to be adapted by Oberai's 3D correction, and a spanwise coherence function of the wall pressure is used to acquire the acoustic pressure for the long span for the experiment.

4.1 Linearized perturbed compressible equations (LPCE)

The linearized perturbed compressible equations can be derived by applying the decomposed state equations (1) to the Navier-Stokes equations, and subtracting the compressible Navier-Stokes equations from them. The LPCE are written in a vector from as,

$$\frac{\partial \rho'}{\partial t} + \left(\vec{U} \cdot \nabla\right) \rho' + \rho_0 \left(\nabla \cdot \vec{u}'\right) = 0 \tag{4}$$

$$\frac{\partial \vec{u}'}{\partial t} + \nabla \left(\vec{u}' \cdot \vec{U}\right) + \frac{1}{\rho_0} \nabla p' = 0 \tag{5}$$

$$\frac{\partial p'}{\partial t} + \left(\vec{U} \cdot \nabla\right) p' + \gamma P \left(\nabla \cdot \vec{u}'\right) + \left(\vec{u} \cdot \nabla\right) P = -\frac{\mathrm{D}P}{\mathrm{D}t}. \tag{6}$$

The LPCE is solved in 2D only, because a 3D approach needs a large dilatation in spanwise direction for resolving the acoustic waves. A 2D method with subsequent correction is more efficient and produces sufficient results. The LPCE is time integrated by a four-stage Runge-Kutta method and spatially discretized by a sixth-order compact finite difference scheme. For damping numerical instabilities a tenth-order spatial filter by Gaitonde et al.[4] is used.

4.2 Computation of Far-Field Sound

The acoustic grid covers a circular domain with a radius of $60D$. The microphones of the experiment are at a distance of $185D$ from the center of the airfoil. The extrapolation is done by a 2D Kirchhoff method in frequency domain given by,

$$4i\hat{p}' = -\int_S \left[\frac{\partial \hat{p}'}{\partial n} H_0^{(2)}(\omega r/c_0) - \frac{\omega}{c_0}(\underline{n} \cdot \underline{r})\hat{p}' H_0^{(2)}(\omega r/c_0)\right] \mathrm{d}S \tag{7}$$

where r is the distance between the Kirchhoff surface and the microphone, $\underline{r}$ its unit vector, c_0 is the ambient speed of sound, $\underline{n}$ a unit vector normal to the Kirchhoff surface, and H the Hankel function. The Kirchhoff surface consists of two circles at $40D$.

According to Oberai[5] the 3D radiated far-field acoustic pressure $\hat{p}'_{3\mathrm{D}}$ at the $z = 0$ plane is related to a 2D predicted acoustic pressure $\hat{p}'_{2\mathrm{D}}$ at the zero spanwise wave number $k_z = 0$ by

$$\hat{p}'_{3\mathrm{D}}(r, \theta, 0, \omega) \approx \hat{p}'_{2\mathrm{D}}(r, \theta, \omega) \frac{1+i}{2} \sqrt{\frac{\omega}{c_0 \pi r}} L_{\mathrm{S}}, \tag{8}$$

with L_{S} as the simulated spanwise length of the iLES.

4.3 Sound Radiation for Long Span

Finally, the acoustic pressure for the simulated span (L_{S}) must be corrected to the actual span L of the experiment. According Kato et al.[6], the sound pressure level (SPL) of a long span can be obtained by adding $10 \log(L/L_{\mathrm{S}})$, if the coherence length L_{C} of the wall pressure is given as $L_{\mathrm{C}} \leq L_{\mathrm{S}}$. For the other case of $L_{\mathrm{C}} > L_{\mathrm{S}}$, the summand $20 \log(L/L_{\mathrm{S}})$ must be added to the SPL of the simulated span. This binary correction was used in many analysis with sufficient results, but here an approach of Perot et al.[7] applying the coherence length with Curle's analogy is used.

First presume a long span object which is divided into N subsections with each the span of L_S, i.e. $L = N \cdot L_{\mathrm{S}}$. The acoustic pressure of the long span $\hat{p}'_{\mathrm{L}}$ and the simulated span $\hat{p}'_{\mathrm{S}}$ are related as $\hat{p}'_{\mathrm{L}} \geq N \cdot \hat{p}'_{\mathrm{S}}$. The relation must be at least equal, but if there are long waves in spanwise direction that can not be resolved by L_{S} then the total acoustic pressure can be greater than the sum of the subsections. The acoustic pressure of the long span in frequency domain can be written as,

$$|\hat{p}'_{\mathrm{L}}|^2 = \hat{p}'_{\mathrm{L}} \hat{p}'^{*}_{\mathrm{L}} \approx \sum_{i=1}^{N} \hat{p}'_i \sum_{i=1}^{N} \hat{p}'^{*}_i = \sum_{i=1}^{N} \sum_{j=1}^{N} \hat{p}'_i \hat{p}'^{*}_j, \tag{9}$$

where $(\,)^*$ indicates a complex conjugate. For proceeding this expression, one need the assumption of statistical homogeneity in spanwise direction which corresponds to the following properties.

1. Every subsection radiates an identical acoustic pressure which is the same as the one of the simulated span $\hat{p}'_{\mathrm{S}}$,

$$|\hat{p}'_1|^2 = |\hat{p}'_2|^2 = \ldots = |\hat{p}'_N|^2 = |\hat{p}'_{\mathrm{S}}|^2. \tag{10}$$

2. The acoustic pressure of each subsection is only lagged by a phase difference which can be expressed by a coherence function,

$$\gamma_{ij} = \frac{|\overline{\hat{p}'_i \hat{p}'^{*}_j}|}{\overline{|\hat{p}'_i|} \cdot \overline{|\hat{p}'^{*}_j|}}. \tag{11}$$

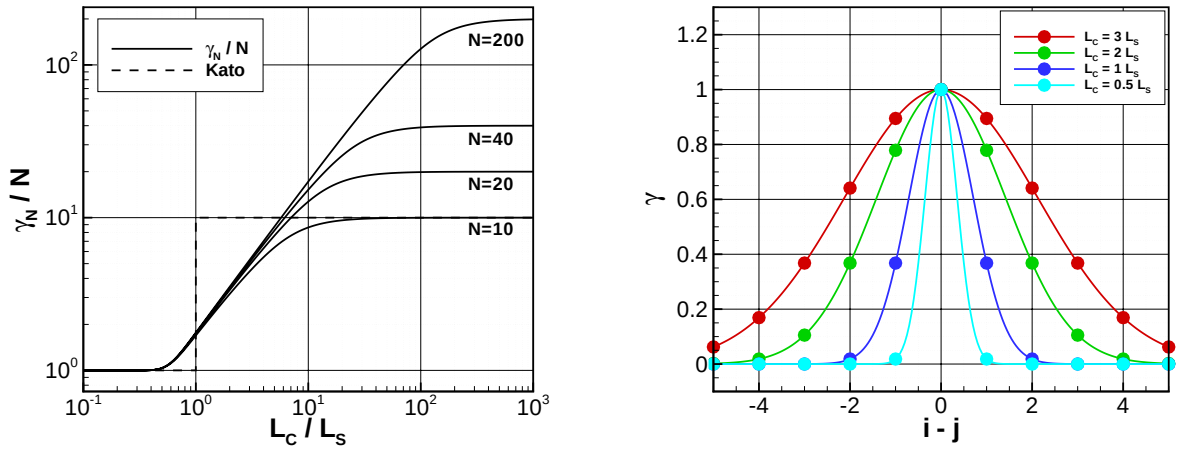

Figure 5: Impact of coherence length L_C, left: proportionality factor γ_N; right: shape of coherence function γ.

3. The coherence function depends only of the spanwise distance between two subsections,

$$\gamma_{ij} = \gamma(\Delta z_{ij}), \qquad \Delta z_{ij} = |z_i - z_j| = |i-j| L_S. \tag{12}$$

The coherence function has the properties of a decay which is similar with a Gaussian distribution[2,8],

$$\gamma_{ij} = \exp\left[-(i-j)^2 \left(\frac{L_S}{L_C}\right)^2\right]. \tag{13}$$

Combining Eq.(9)-(13) leads to a final relation between the acoustic pressure of long span to simulated span,

$$|\hat{p}'_L|^2 = |\hat{p}'_S|^2 \underbrace{\sum_{i=1}^{N}\sum_{j=1}^{N} \exp\left[-(i-j)^2 \left(\frac{L_S}{L_C}\right)^2\right]}_{\gamma_N}. \tag{14}$$

The proportionality factor γ_N has a range from N to N^2, which corresponds to the correction by Kato. Graphs of γ_N against the coherence length L_C is plotted in Figure 5 left. If $L_C/L_S < 0.4$ then $\gamma_N = N$ which corresponds to the Kato summand of $10\log(L/L_S)$. The other extreme is when $L_C/L_S > 2L$ then $\gamma_N = N^2$ which fits to Kato's upper limit of $20\log(L/L_S)$. The domain in between is characterized by a linear distribution in logarithmic scale.

The limit at $0.4L_C/L_S$ can be explained with the shape of the Gaussian coherence function in Figure 5 right. The coherence function γ_{ij} in Eq. (13) is evaluated at integer

values of $|i-j|$ only, at the filled circles. The value for $i-j=0$ is always one, but the function decays very quickly. Hence, a neighbor is just affected for coherence lengths over $0.4L_C/L_S$.

The measuring of γ_{ij} as function of acoustic pressures between subsections is hardly possible. Another available source is a spanwise coherence function of the wall pressure. Figure 6 right shows the coherence at the maximum thickness of the airfoil, $x/D = 2.95$. The coherence length L_C as sole parameter in γ can be obtained by a regression. It is apparent that the coherence depends strongly of the frequency / Strouhal number.

The question of where to measure the wall pressure coherence is more interesting. Figure 6 left shows the coherence length distribution over the whole spectra for different locations, rod ($x/D = -10.4$), leading edge ($x/D = 0.2$), maximum thickness of airfoil ($x/D = 2.95$), 60% of airfoil ($x/D = 6$) and trailing edge ($x/D = 9.7$). The left side of the spectra with its high peaks can be ignored, because these are just artifacts of the averaged Fourier analysis. All graphs have a peak at the vortex shedding frequency, except for the trailing edge, here is no significant coherence at all. The strongest coherence $L_C/D = 10$ is at the leading edge where the flow is still laminar and the pressure waves are most two-dimensional. If the waves would be perfectly 2D then the coherence length would be infinite long. At rod and maximum thickness of airfoil is $L_C/D = 5$, and more downstream the value decreases. The model considers just one distribution for the whole domain. So one has to decide for a distribution that represents the area best. The values of the maximum thickness of the airfoil seem to be a reasonable choice, because the airfoil's laminar part is rather small. The value of 5 fits also well with the data from experiments[2]. The correction has only an impact to a small bandwidth around the shedding frequency. The higher frequencies' coherence length is too short ($L_C/D < 1$ equals to $L_C/L_S < 0.33$) to have any effect.

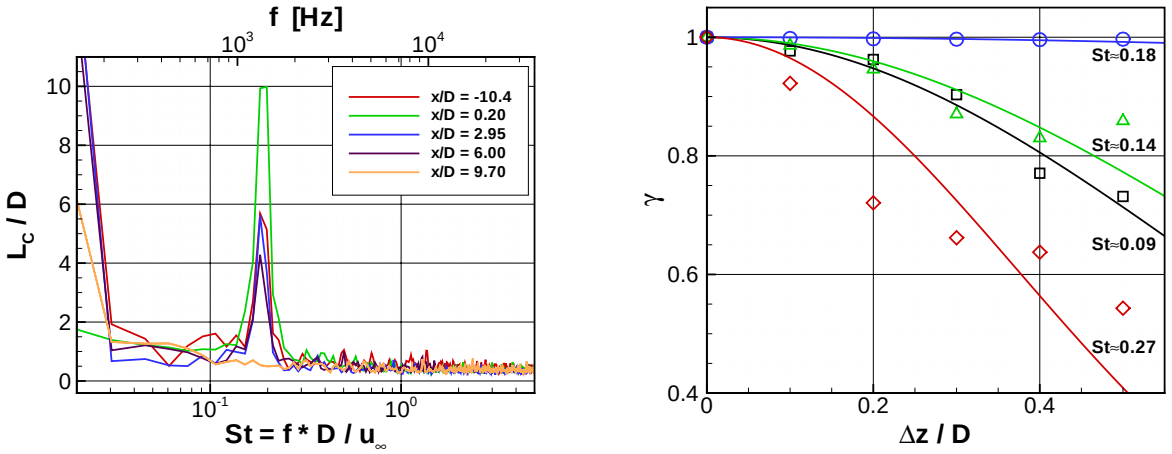

Figure 6: Coherence as function of frequency, left: coherence length at different positions, $x/D = 0$ matches the leading edge; right: regression at $x/D = 2.95$.

4.4 Comparison with experiment

The experimental data in this study was obtain by Jacob from Ecole Central de Lyon[2] who performed a very similar test case. The experiments produced extensive data which was used for comparison, but only some part is shone in this work. Comparisons are done for velocity profiles, velocity spectra at certain points and power spectral densities (PSD) in the far-field.

4.4.1 Velocity profiles

All data for the velocity profiles were obtained from mid-span plane. The experimental data was measured by a hot wire. The mean velocity U_{AVE} was acquired by averaging flow data over a time span of 50 cycles of Karman vortex shedding. The U_{RMS} used the same data length, but is was measured on certain positions only which means there is no continues distribution. The locations of the profiles can be seen in Figure 7(a), it covers the rod 7(b), the near rod wake 7(c), the far rod wake 7(d), the leading edge 7(e) and the near airfoil wake 7(f).

Figure 7 (b) shows the effect of the rod. The experiment and the simulation match very well the slope of the velocity distribution caused by the blocking of the cylinder. The blocking effect still exists at $y/D = 10$ of 0.5 % velocity excess which is better captured by the LES than experiment. Towards the distance of $y/D = 15$ the experiment increases its velocity which is caused by the design of the wind tunnel. It is a free stream anechoic wind tunnel that generates a rectangular jet. The wet area of the jet's potential core ends at $y/D = 15$. Hence, the flow is biased by fringe effects of the jet with the surrounding medium.

The near wake of the rod seems a bit surprising. On the one hand the fluctuations are overpredicted, Figure 7 (c) left, while on the other hand the velocity wake is too deep, Figure 7 (c) right, which would indicated a too small mixing of the flow. The mixing is ruled by the large scale and sub scale fluctuations. No sub scale turbulence model was implemented in the LES which suggest that this part of the flow is governed by sub scale turbulence. But one has to notice that the prediction of the strength of a rode wake is always a challenging task. In Figure 7 (c) left the two initial rod shear layers can still be guessed, which contain vortex sheds at each side.

In Figure 7 (d), the results in the rod's far wake match very well in terms of fluctuations and velocity deficits. The wake becomes wider and the fluctuations decrease. The only significant difference is a shift of $0.2D$ upward of the experimental wake. Jacob reasons it with the experimental setup, where the center of the rod and the mid chord of the airfoil have an offset of $0.2D$. The LES uses just half of it, $0.1D$, and it has no visible effect.

Figure 7 (e) displays the flow a quarter chord length behind the leading edge. The fluctuations agree quite well, but the velocities have an offset. The shape of the distribution looks fine and similar, but the LES overpredicts the velocity magnitude of about 6 % in terms of u_∞. The small bump at $x/D = 3$ in the LES results from an high order stencil

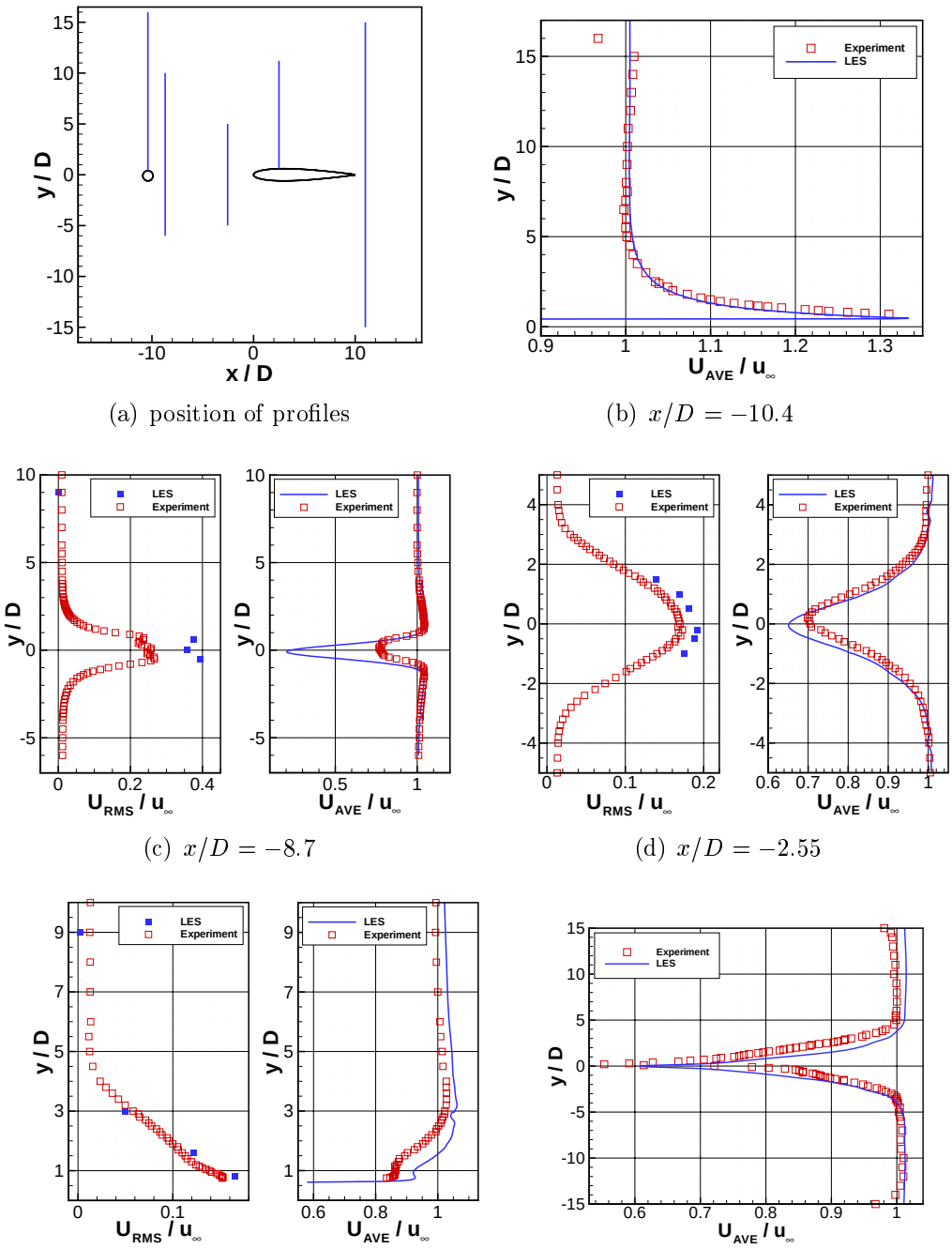

(a) position of profiles

(b) $x/D = -10.4$

(c) $x/D = -8.7$

(d) $x/D = -2.55$

(e) $x/D = 2.5$

(f) $x/D = 11$

Figure 7: Velocity profiles of LES and experiment.

grid effect that was convected to this position.

The last comparison, Figure 7 (f), shows the velocity profiles in the near wake of the airfoil. The magnitudes of simulation and experiment fit very well, but there is a vertical

shift in the wake of the experiment again.

4.4.2 Velocity spectra

The comparison of velocity and fluctuation profiles clarified that the simulation captured the physics of the flow. Hence, it is possible to compare other statistical properties. One aspect is to investigate the origin of the fluctuations. Determining the velocity spectra S_{uu} at certain locations might lead to its source. In the experiment, it is easy to capture a long time history of data which is used in an averaged Fourier analysis and still has a good spectral resolution. While the simulation always has the problem of computational time. It is imperative to use an averaged Fourier analysis, otherwise the results are overlaid by too much noise. The experiment has a spectral resolution of $\Delta f = 4\,\mathrm{Hz}$ after some hundred averagings, while the simulation has a spectral resolution of $\Delta f = 79\,\mathrm{Hz}$ after 6 averagings. This coarse resolutions means that output for less than 720 Hz (St=0.1) is not reliable and can be ignored.

Figure 8 (a) visualizes the locations of the recording. There are too many positions to show results for all of them. Only position 2, 3, 8 and 13 are shown here in Figure 8 (b)-(d). Every figure has a peak at $St = 0.19$ which indicates that the fluctuations are mainly due to vortex sheds. The LES predicted peaks are always at a slightly too low frequency, but the rest agrees very well. In Figure 8 (b), the fundamental frequency has a very strong peak while the first harmonic is very weak. This position is mainly influenced by the rod's upper shear layer. A bit more down at the x-axis (Figure 8 (d)) the fundamental peak and the first harmonic have the same magnitude and even another harmonic is visible. This location is equally influenced by the vortex sheds of both sides of the rod. More downstream at position 8 the magnitude of the main peak decreases, but the first harmonic is visible which means that both vortex sheds pass this point. Behind the leading edge in Figure 8 (e) the peak increases due to the acceleration effect of the airfoil, but the first harmonic peak is detectable, too. One reason is that some vorticity is convecting to the opposite side of the airfoil. Another is that also the pressure fluctuates because of the incoming fluctuations. Figure 9 depicts a power spectrum density (PSD) of the wall pressure in that region, and it clearly shows peaks for the fundamental and harmonic frequency. The results of the LES (Peth) overpredicts slightly the noise level, and the harmonic peak can only be guessed, but it matched well with a LES by Jacob[2] the same author as of the experiment. All this proves that the vortex shedding is ruled by the low frequency eddies predicted by the LES.

4.4.3 Sound pressure level spectra

The computational methodology for obtaining the far-field was described above. The microphones are positioned in a distance of $185D$ from the airfoil center (half chord downstream of the leading edge) in mid-span plane. In the experiment Jacob[2] found that the wind tunnel's noise is dominant for $St < 0.05$ by testing flow only, rod only and

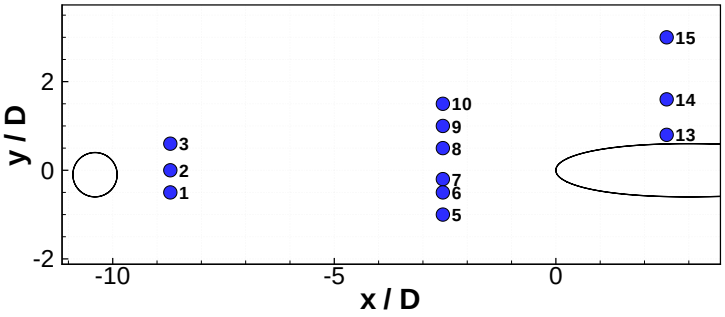

(a) position of probes

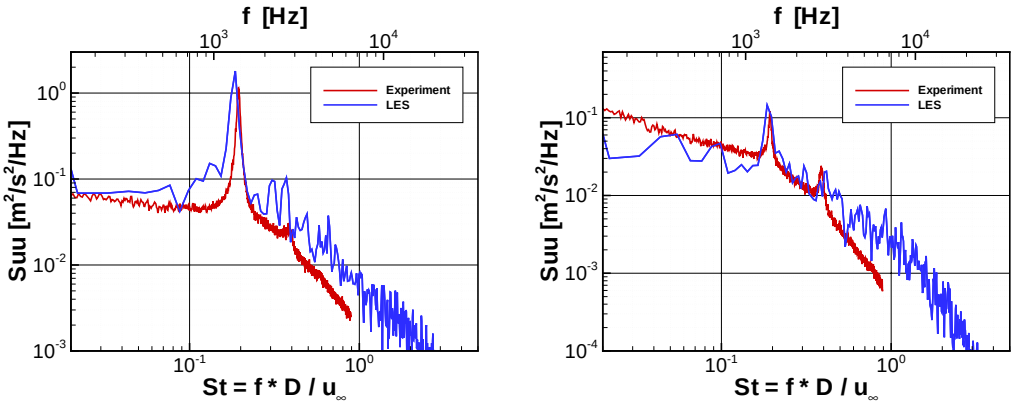

(b) position 3

(c) position 8

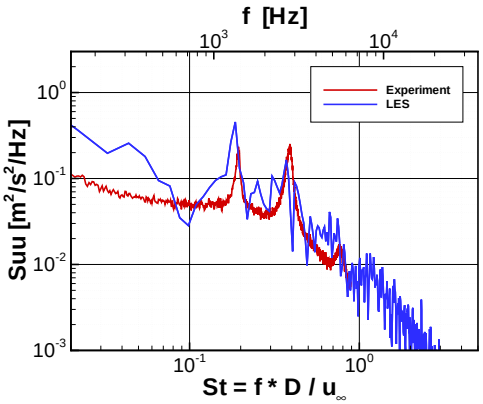

(d) position 2

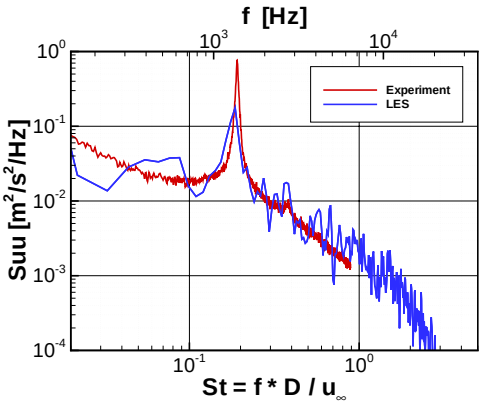

(e) position 13

Figure 8: Velocity spectra S_{uu} versus Strouhal number St at different locations.

rod & airfoil. His data acquisition is carried out with a spectral resolution of 4 Hz and the number of averages is 200. The simulation uses just 6 averages and has a spectral resolution of 84 Hz.

Figure 10 (a) shows a sketch of the location of the microphones in relation with the

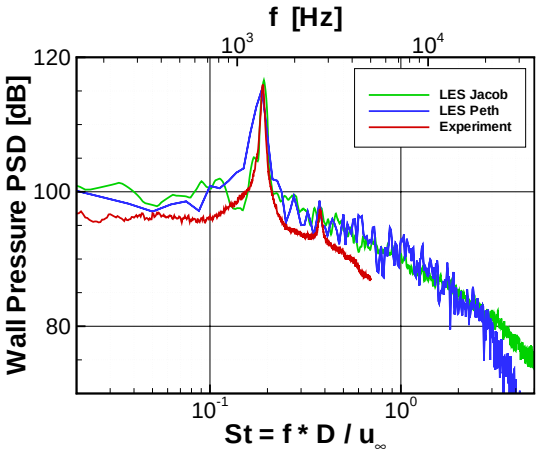

Figure 9: Wall pressure PSD at $x/D = 2$.

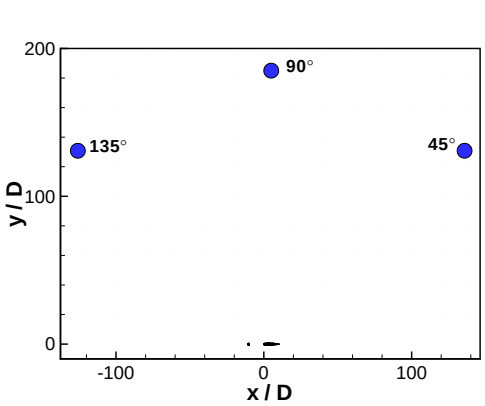

(a) position of microphones

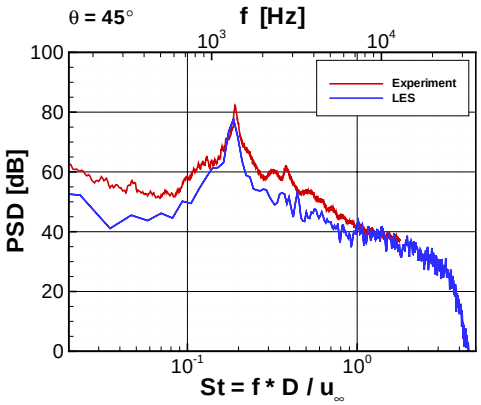

(b) observation at 45°

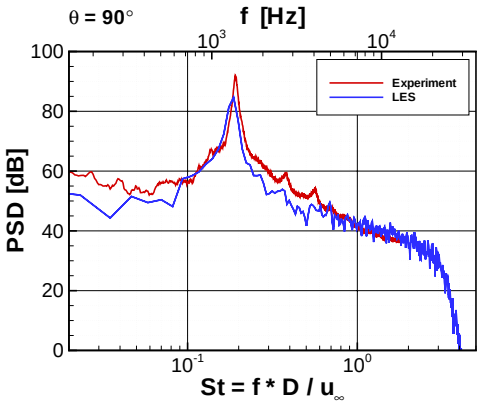

(c) observation at 90°

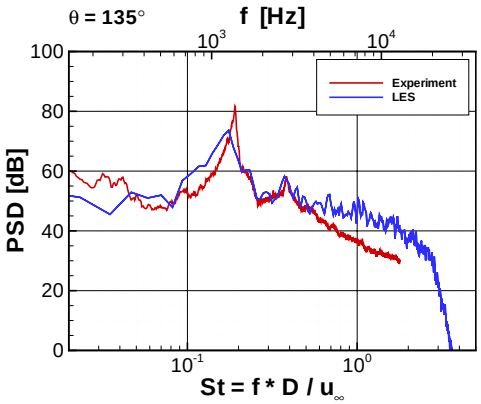

(d) observation at 135°

Figure 10: Far-field acoustic PSD for 3 different observation angles.

rod-airfoil configuration. There are comparisons for three different positions, 45°, 90° and 135°. The LES predicts the peak of the shedding frequency accurately. Its frequency is slightly too small, but its magnitude is always underpredicted by 5 to 7 dB. The overall shape of the distributions agrees well, it just looks like the overall level of the simulation is too low. But this discrepancy is not constant for all angles. At 45° the offset seems to be biggest, while at 90° it is significantly smaller. And at 135° the first harmonic peak is perfectly predicted, but the fundamental peak fits poorly which is maybe caused by the coarse spectral resolution. If all simulated distributions would be shifted to the experimental data then one could see that there is a hump at high frequencies $St > 0.6$. One reason could be that the LES resolves smaller scales than the experiment[2]. Also the signal proceeding is not optimal in terms of spectral resolution and averagings. It is also possible that the quality of the hydrodynamic and acoustic grid cause the deviation. The broadband noise is strongest at 45° and decreases for increasing angles. This is an indication that the dominant source for the broadband noise is at the trailing edge.

5 CONCLUSION

The various comparisons of hydrodynamic and aeroacoustic results with the experimental data show that the computational methodology used in the present study is reasonably consistent and accurate. Some discrepancy observed in the computational results is primarily due to the grid resolutions for both flow and acoustics. One other possibility is that any form of sub-grid scale model was not used in the present LES. The simulation pointed out that the whole flow field and tonal noise are governed by the vortex shedding of the rod. The generation mechanism of the tonal noise is the swinging of the stagnation point around the leading-edge of the airfoil through periodic interactions of the Karman vortex with the airfoil. The broadband noise is generated by several sources: turbulent wakes between the rod and the airfoil (large amount of volume sources), their interaction with the airfoil leading-edge, and the trailing-edge scattering of the eddies within the boundary layers over the airfoil. The spanwise coherence functions of the wall pressure are rapidly decaying in most frequencies, except at St=0.2. Thereby, the spanwise coherence lengths are smaller than the rod diameter in most cases but at St=0.2, L_c is four or five times the rod diameter widely over the airfoil surface.

REFERENCES

[1] J. H. Seo and Y. J. Moon, *Linearized Perturbed Compressible Equations for Low Mach Number Aeroacoustics*, J. Compt. Physics (in review), also 11th AIAA/CEAS Aeroacoustics Conference, AIAA-2005-2927, (2005).

[2] M. C. Jacob, J. Boudet, D. Casalino and M. Michard, *A Rod-Airfoil Experiment as Benchmark for Broadband Noise Modelling*, Theoret. Comput. Fluid Dynamics, Vol.

19, pp. 171-196, (2005).

[3] S. K. Lele, *Compact Finit Difference Schemes with Spectral-like Resolution*, Journal of Computational Physics, Vol. 103, (1992), pp. 16-42.

[4] D. Gaitonde, J. S. Shang and J. L. Young, *Practical Aspects of Highorder Accurate Finite-Volume Schemes for Wave Propagation Phenomena*, International Journal for Numerical Methods in Engineering, Vol. 45, No. 12, (1999), pp. 1849-1869.

[5] A. A. Oberai, F. Roknaldin and T. J. R. Hughes, *Trailing-Edge Noise due to Turbulent Flows*, Technical Report, Boston University, Report No. 02-002, (2002).

[6] C. Kato, A. Iida, Y. Takano, H. Fujita, M. Ikegawa, *Numerical Prediction of Aerodynamic Noise Radiated from Low Mach Number Turbulent Wake*, AIAA paper 93-145, (1993).

[7] F. Perot, J. M. Auger, H. Giardi, X. Gloerfelt, C. Baily, *Numerical Prediction of the Noise Radiated by a Cylinder*, AIAA-Paper 2003-3240, (2003).

[8] D. Casalino and M. Jacob, *Prediction of Aerodynamic Sound from Circular Rods via Spanwise Statistical Modelling*, Journal of Sound and Vibration, Vol. 262, No. 4, (2003), pp. 815-844.

[9] E. Sorgüven, F. Magagnato, M. Gabi, *Acoustic Prediction of a Cylinder and Airfoil Configuration at High Reynolds Numbers with LES and FHW*, ERCOFTAV Bullentin **58**, 47-50, (2003).

[10] F. Magagnato, E. Sorgüven, M. Gabi, *Far Field Noise Prediction by Large-Eddy Simulation and Ffowcs-Williams and Hawkings analogy*, AIAA paper 2003-3206, (2003).

[11] V. Strouhal, *Über eine besondere Art der Tonerregung*, Ann. Phys. Chem. **3**(5), pp. 216-251, (1878).

[12] J. Boudet, D. Casalino, M. C. Jacob, P. Ferrand, *Prediction of Broadband Noise: Airfoil in the Wake of Rod*, AIAA paper 2004-0852, (2004).

[13] H. Glauert, *The Force and Moment on an Oscillating Airfoil*, British Academic Research Collaboration, R. & M., No. 1242 (1929).

[14] M. E. Goldstein, H. M. Atassi, *A Complete Second Order Theory for the Unsteady Flow about an Airfoil due to a Periodic Gust*, Journal of Fluid Mechanics **74**(4), pp. 741-765, (1976).